European Conference on Computational Fluid Dynamics
ECCOMAS CFD 2006
P. Wesseling, E. Oñate and J. Périaux (Eds)

NUMERICAL STUDY OF THE UNSTEADY FLOW STRUCTURES AROUND TRAIN-SHAPED BODY SUBJECTED TO SIDE WINDS

Hassan Hemida* **and Siniša Krajnović†**

*Chalmers University of Technology
Division of Fluid Dynamics, Department of Applied Mechanics
412 96 Gothenburg, SWEDEN
e-mail: hemida@chalmers.se
web page: http://www.tfd.chalmers.se/∼ *lada/projects/sidewind/proright.html*
†Chalmers University of Technology
Division of Fluid Dynamics, Department of Applied Mechanics
412 96 Gothenburg, SWEDEN
e-mail: sinisa@chalmers.se

Key words: Fluid Dynamics, Wake structures, High speed trains, Side winds, LES

Abstract. *Large-eddy simulation (LES) is made to investigate the flow around a generic train under side wind conditions. Two different side-wind yaw angles are used in the investigation:* 35^o *and* 90^o*. The Reynolds numbers based on the height of the train and the freestream velocity are* 3×10^5 *and* 3.7×10^5 *for the* 90^o *and* 35^o *yaw angles, respectively. Two computations on two different meshes are made for each simulation in order to check the effect of the mesh resolution on the results. The fine and the coarse meshes give similar results for each simulation meaning that the results are mesh independent. The results are also verified against experimental data that have been collected on the numerical model at the same Reynolds number. Good agreement is obtained between the LES results and the experimental data. The LES results showed that the flow around the train at* 90^o *yaw angle is dominated by unsteady vortex shedding. The large-scale instability associated with the shedding of large-scale vortices from the recirculation region to the far wake flow and the small-scale instability associated with the small-scale Kelvin Helmholtz instability are yielding highly unsteady flow. The LES results for the* 35^o *side-wind yaw angle show that two flow regimes exist in the wake. The first flow regime is represented with the steady vortex lines in the upper part of the wake flow. It changes into unsteady shedding after some distance from their onset on the surface of the train. The second flow regime is the unsteady movement of the lower part of the wake vortices which attach and detach from the surface of the train in a regular fashion. The influence of side wind yaw angle and the wake structures on the aerodynamic coefficients is discussed in the paper. The paper gives a picture of the unsteady flow and its instabilities around trains at large and low yaw angles.*

1 INTRODUCTION

The new generation of high-speed trains is light in weight in order to provide high acceleration and to reduce the energy necessary to overcome gravity and friction forces. When these trains cruise in a strong side wind, there is a stagnation region with high pressure on the streamwise face while a region of low pressure is formed on the lee side due to the recirculation regions in the wake flow. In addition, the flow moves over the train roof at high velocity, making a region of low pressure on the upper side of the train. Due to these pressure differences, the high-speed trains experience strong aerodynamic forces and moments such as side and lift forces and a turning moment, as shown in Fig. 1. In such conditions, the high-speed trains are at high risk of overturning or derailment.

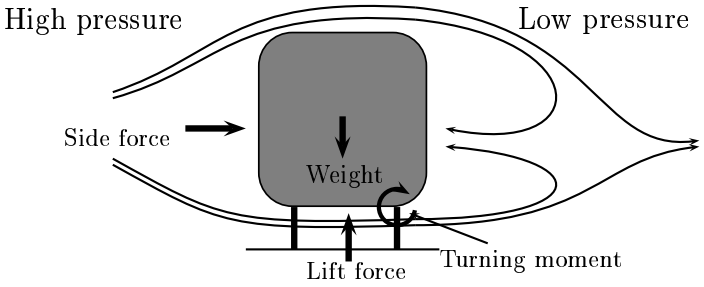

Figure 1: Aerodynamic forces and moments due to side winds

It is well known that the shape of the vehicles of the train determine by high extend the influence of the side winds on the stability of the train. Thus the vehicle's side wind resistance can be improved by adjusting its design. Previous experimental studies have concentrated mainly on the vehicle's response to the side wind and not much on understanding the flow mechanisms. Prevention of the unwanted influences of a side wind requires that flow structures on the train surface and around it are fully understood in both the instantaneous and the time-averaged flow. Unsteady flow past a train in a side wind has been the object of numerous experimental investigations[1–7] . The primary interest in these investigations was the measurement of some integral parameters such as drag, lift and side force coefficients together with measurements of the natural wind characteristics around the train. Some other researchers have investigated the flow structures numerically[8,9] to obtain a better understanding of the flow behavior. Most of these studies are based on Reynolds-averaged Naiver-Stokes (RANS) equations or time varying RANS (URANS). Here only the mean flow is explored and the instantaneous information is lost. Since the side-wind instability is a consequence of the unsteadiness of the flow field around the train, an accurate time-dependent solution is necessary. In this paper, large-eddy simulation is made to solve the flow around a generic train model subjected to side winds at two different yaw angles: 90^o and 35^o. Based on the height of the train and the freestream velocity, the Reynolds numbers were 3×10^5 and 3.7×10^5 for 90^o and

35^o yaw angles, respectively. These values for Reynolds number are typically the same as the experimental Reynolds numbers. The aim is to investigate the unsteady behavior of the wake structures and its influences on the aerodynamic forces.

2 THE INFLUENCES OF REYNOLDS NUMBER

Copley[5] investigated the influence of Reynolds number on the flow field around a train when it is subjected to a cross wind. He found that, for very low Reynolds number, the flow around the train is laminar everywhere and remains attached to the train surface. Increasing the Reynolds number results in a separation on the roof-side streamwise edge and the detachment of the flow from the face, as shown in Fig. 2a. At the same time, the wake begins to shed vortices in a regular fashion. A further increase in Reynolds number makes the flow fully turbulent in the wake and in the separation region over the roof-side face. At some critical Reynolds number, the flow reattaches to the face, forming a separation bubble, as shown in Fig. 2b. For higher Reynolds number, this separation bubble is suppressed and the flow over the roof-side face is fully attached, as shown in Fig. 2c.

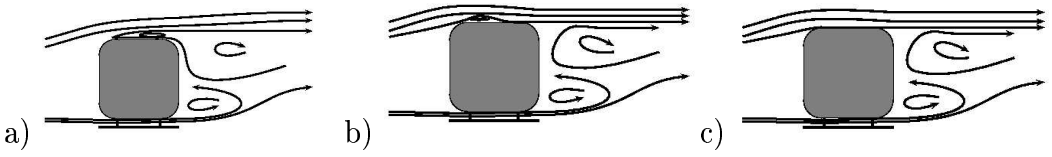

Figure 2: Reynolds number effect on the flow structures around train under cross-wind conditions.

The value of the critical Reynolds number depends very much on the shape of the train and on the direction of side winds[10]. It depends also on the roughness of the surface of the train. The roughness of the surfaces helps to produce a turbulent boundary layer that occurs at lower Reynolds number than that for smooth surfaces. Because of that, a trip wire is always attached to the top-side face in the experimental investigation of side wind flow around trains. It helps to produce a turbulent boundary layers at low Reynolds number similar to real trains. Once reattached flow is formed on the roof-side face, the aerodynamic coefficients are believed to be Reynolds number independent.

3 FLOW INSTABILITIES AROUND TRAINS

Numerical and experimental studies of the flow around bluff bodies[11−15] show that such flows are highly unsteady and three-dimensional. Moreover, when the Reynolds number is high enough to obtain a fully turbulent flow in the shear layers and in the wake, two main instability modes are present in the wake flow. The first is the large-scale shedding in the wake, and it manifests itself as a progressive wave motion with alternate fluctuations produced by the shear present at the limit between the recirculation zone and

the exterior fluid. These fluctuations determine the periodic shedding of the vortices that form behind the bluff body. The second high frequency mode is so called spiral mode, which is associated with the small-scale shear-layer Kelvin-Helmholtz instability on the periphery of the recirculation region where shear flow is present, as shown in Fig. 3. This instability is responsible for the distortion of the large vortex structures, shedding of the vortex tubes in a quasi-coherent fashion inside the detached shear layers, production of the small scales, and, eventually, transition to turbulence in the wake (for more detail see[15]). The high frequency mode is very important in determining the shape of the flow structures and hence the aerodynamic forces. Any solution method used to investigate the influences of side wind should be able to capture the two different instability modes in the flow.

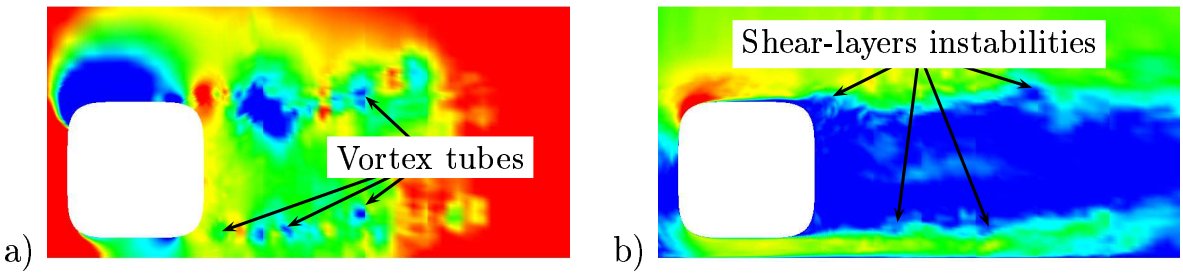

Figure 3: Cross-section of the LES flow around trains in a cross-wind showing the shear-layer instabilities colored by (a) the instantaneous static pressure and (b) the magnitude of the instantaneous velocity vector.

4 SOLUTION METHOD

Capturing the small flow structures around trains and investigating the flow features require simulation methods that resolve, rather than model, the main dynamics governing the flow. Numerical solutions using URANS are not able to catch the high frequency modes since the Reynolds stresses representing the turbulence in URANS are modeled with a turbulence model. Finding a true representation of the flow is dependent on the turbulence model used. Moreover, it is difficult to define a model that can accurately represent the Reynolds stresses in the region of separated flow, such as the wake behind a train. Direct Numerical Simulation (DNS) is very expensive and it is not feasible nowadays to solve the flow around trains even for relatively low Reynolds number. In this paper large-eddy simulation is used to solve the flow. It is an intermediate method between DNS and RANS. In LES, the large eddies are computed directly and the influences of the small-scale eddies on the large-scale eddies are modeled. The incompressible Navier-Stokes equations and the continuity equation are filtered using an implicit spatial filter.

The resulting filtered equations are:

$$\frac{\partial \bar{u}_i}{\partial t} + \frac{\partial}{\partial x_j}(\bar{u}_i \bar{u}_j) = -\frac{1}{\rho}\frac{\partial \bar{p}}{\partial x_i} + \nu \frac{\partial^2 \bar{u}_i}{\partial x_j x_j} - \frac{\partial \tau_{ij}}{\partial x_j} \tag{1}$$

and

$$\frac{\partial \bar{u}_i}{\partial x_i} = 0. \tag{2}$$

Here, $\bar{u}_i$ and $\bar{p}$ are the resolved filtered velocity and pressure, respectively, while $\tau_{ij} = \overline{u_i u_j} - \bar{u}_i \bar{u}_j$ are the sub-grid scale (SGS) stresses. The sub-grid scale stresses represent the contribution of the small unresolved scales to the large resolved ones. These are unknown and must be modeled. The Smagorinsky model is used in the present work to model the SGS stresses because of its simplicity and in order to reduce computational cost. It models the SGS stresses as:

$$\tau_{ij} - \frac{1}{3}\delta_{ij}\tau_{kk} = -2\nu_{sgs}\bar{S}_{ij} \tag{3}$$

where $\bar{S}_{ij}$ is the resolved rate of strain defined as:

$$\bar{S}_{ij} = \frac{1}{2}\left(\frac{\partial \bar{u}_i}{\partial x_j} + \frac{\partial \bar{u}_j}{\partial x_i}\right) \tag{4}$$

and ν_{sgs} is the SGS viscosity defined as:

$$\nu_{sgs} = (C_s f \Delta)^2 \mid \bar{S} \mid . \tag{5}$$

Here, $\mid \bar{S} \mid = (2\bar{S}_{ij}\bar{S}_{ij})^{1/2}$, C_s is the SGS model coefficient and f is the van Driest damping function that has the form:

$$f = 1 - exp\left(\frac{y^+}{25}\right). \tag{6}$$

The value of the SGS model coefficient, C_s, is 0.1 in the present work. Since the resolved strain-rate tensor, $\bar{S}_{ij}$, does not vanish at the wall, the value of the coefficient, C_s, should be adjusted to take partially into account the effect of the wall. Thus, the damping function, f, is used to damp the turbulence length-scale next to the wall. The same model constant has been used in simulations of the flow around simplified road vehicles[16,17]. The filter width, Δ, is taken as the cubic root of the volume of a finite volume cell.

5 NUMERICAL IMPLEMENTATIONS

Two computations on two different computational grids were made at each yaw angle in order to investigate the influence of the mesh resolution on the results and to establish numerical accuracy. The ICEM-CFD commercial grid-generator package was used to create the meshes. In this work, the numerical flow predictions were carried out using an in-house finite volume developed multi-purpose package CALC-PVM for parallel computations of turbulent flow in complex multi-block domains. LES equations were discretized using a three-dimensional finite volume method in a collocated grid arrangement using Rhie-Chow interpolation. The convective, viscous diffusion plus sub-grid fluxes were approximated by second-order-accurate central difference scheme. To reduce the numerical dissipation, no upwind schemes were used in the simulations. Because of that, the mesh stretching ratio was kept below 1.1 around the train models since the central difference scheme is more sensitive to the stretching ratio, especially in the places where large flow variations are expected (close to the train model and in the wake where the flow is highly unsteady). The time integration was done using the Crank-Nicolson second-order scheme. The SIMPLEC algorithm was used for the pressure-velocity coupling. Additional details about this code can be found in[18].

6 COMPUTATIONAL MODEL AND BOUNDARY CONDITIONS

The train model used in this paper is the one of Copley[5]. The cross-sectional profile of the idealized train model was defined by the following equation

$$\mid y \mid^n + \mid z \mid^n = c^n. \tag{7}$$

The model consists of two parts, a train body and a nose (see Fig. 4a). The train body has a cylindrical shape with a height of $D = 125mm$ and a total length of $9.36D$. The profile of the cross section follows Eq. 7, in which the value of $c = 62.5mm(D/2)$ and $n = 5$. This model is chosen due to its simplicity and the existence of experimental data. The computational domain is shown in Figure 4. The train model is mounted in a closed channel (wind tunnel) as shown in Fig. 4a. The channel has an extension of $29D$ in the streamwise direction, a height of $9.76D$ and a width of $13.4D$. It has walls at all sides except the inlet and the outlet. Similar to the experimental set-up, our train model is mounted horizontally on the wind tunnel side wall. The distance between the model and the ground is chosen to be $0.15D$, which is typical for real trains. The model center-line position is chosen to be $8D$ from the inlet and $21D$ from the outlet of the numerical wind tunnel. These lengths were found sufficient in previous LES of flows around similar bodies[11,19].

The inlet plane is kept parallel to the train in each simulation to ensure constant boundary layer thickness approaching the train surface.

The flow enters the channel with uniform velocity constant in time. No-slip boundary conditions are used on the train body and floor. Wall functions are used on the lateral walls

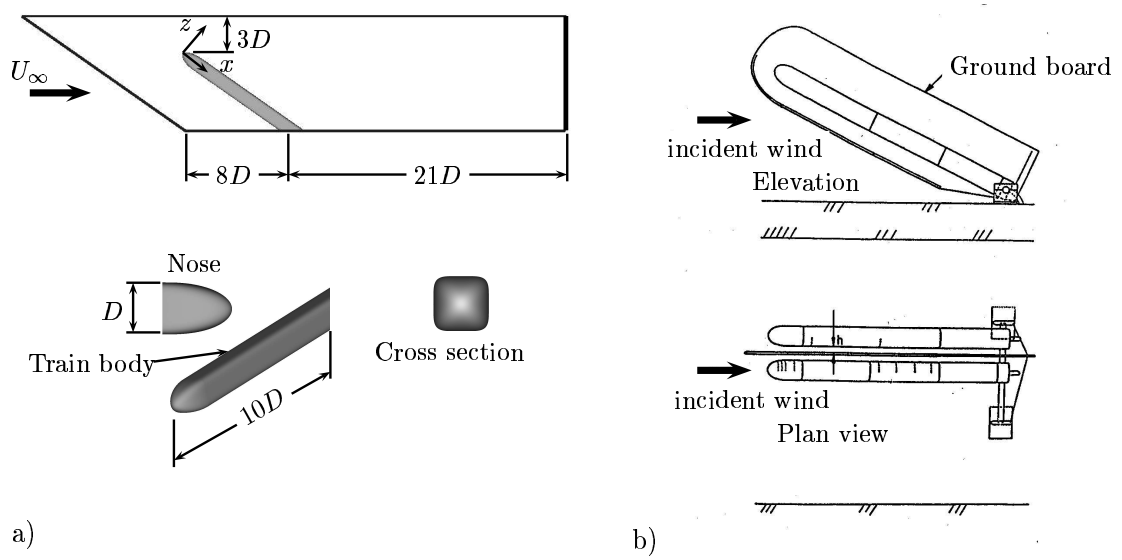

Figure 4: Computational domain and simplified model. (b) Experimental set-up for the 35^o yaw angle.

and roof. Convective boundary conditions are used at the channel exit. Homogeneous Neumann boundary conditions are used for the pressure at all boundaries.

7 NUMERICAL ACCURACY

Two computations with different numbers of nodes are made for each yaw angle. The fine meshes contain 11 and 14 million nodes and the coarse meshes contain 8 and 6 million nodes for the 90^o and 35^o yaw angles, respectively. The ICEM-CFD commercial grid-generator package was used to create both the model geometries and the meshes around them. The train model was constructed using Eq. 7. Another dummy train with a height equal to $1.15D$ is built around the model. The ICEM-CFD Hexa package was employed to generate a hexahedral mesh around the previously described model. An O-type mesh was made in the belt of thickness of $0.075D$ between the model and the dummy train. This allows the generation of a smooth mesh in all directions, see Fig. 5a. Figure 5a also shows another O-type mesh of a thickness of $0.5D$ (in the coarse mesh) and $0.1D$ (in the fine mesh) that is made around the first O-type mesh. The dummy train surface is used as a shared surface between the two O-type meshes. Figure 5b shows the mesh shape around the nose of the train and one block under the train (block U), which is enclosed between the second O-type mesh and the groundboard. The rest of the blocking structures were made using H grids. Hyperbolic stretching is used to make a finer mesh close to the train model and a coarser mesh in the regions away from the train. The total number of nodes are 11.5 and 8 million for the fine mesh and the coarse mesh, respectively. The time-averaged data are collected using 100,000 time steps. This corresponds to a total simulation time of 10 sec ($t^* = tU_\infty/D = 80$). These data are used to explore the time-averaged flow around train models. Mesh dependency is

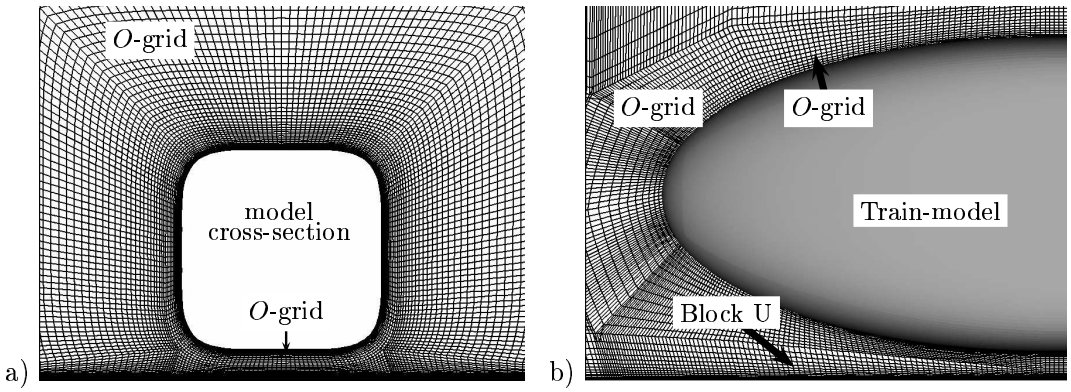

Figure 5: Coarse mesh (a) Cross section of the mesh shows the first and the second O-grids around the train model (b) Mesh shape around the train nose in the symmetric $x-y$ plane of the train.

shown in Fig. 6. The coarse and fine meshes give similar results for the time-averaged pressure distribution. Further refinement of the meshes does not influence the results much. Comparison of the LES results with the experimental data is also shown in Fig. 6. Good agreement is obtained between LES results and the experimental data in the case of the 90^o yaw angle. Figure 4b shows the experimental set-up used for the 35^o yaw angle, which is different from our set-up. In the experiment, two models are used (one is a mirror model to the other one used for measurements) to simulate the relative motion of the train with respect to the ground. In addition, a trip wire is used to suppress the separation on the roof-side face. Figure 6b shows that the LES results for the 35^o yaw angle suffer from these differences between the two set-ups. The LES overestimates the pressure under the body due to the difference between the LES and the experimental set-ups. LES shows an underestimated pressure on the roof-side face due to the flow separation. Good agreement is obtained on the other faces of the model.

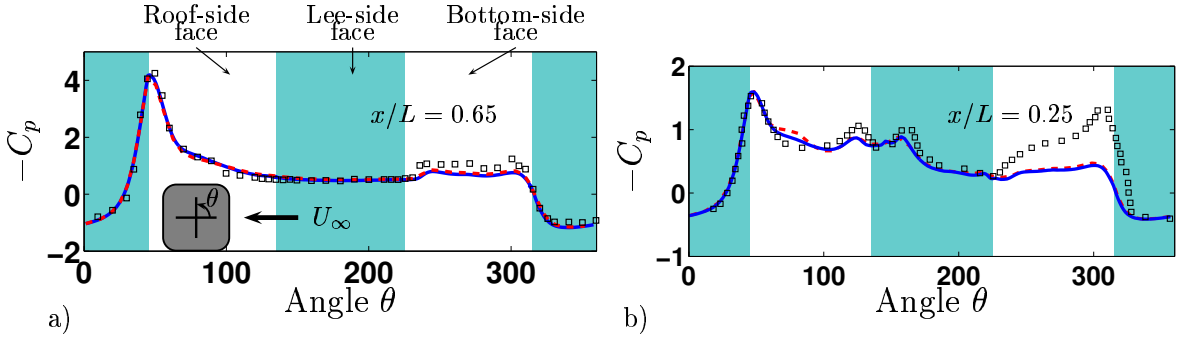

Figure 6: Local pressure coefficient. (a) 90^o yaw angle. (b) 35^o yaw angle. LES using fine mesh (solid line); LES using coarse mesh (dashed line); experimental data (symbols).

Since the model is attached to the side wall in the simulations, a stagnation region

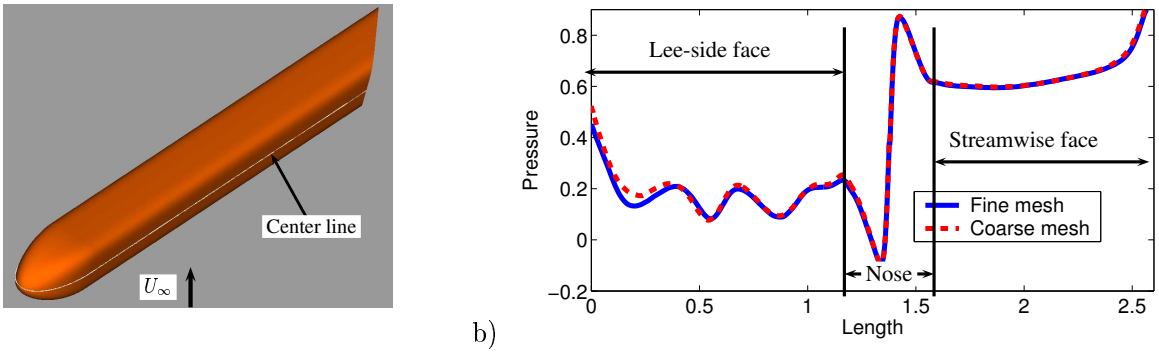

Figure 7: a) Train model. b) Time-averaged pressure distribution along the train centerline shown in figure 7a.

is formed between the model and the side wall in case of 35^o side wall yaw angle. This stagnation region results in an increase in the pressure on the streamwise face along the train length in the direction of the side wall. The experimental model is not attached to the side wall in case of 35^o side-wind yaw angle, where the influence of the side wall was limited to a region extending $4D$ from the side wall. Figure 7b shows the LES pressure distribution along the center line of the train. The centerline of the train is shown in Fig. 7a.

8 RESULTS

In the case of the 90^o yaw angle, the two vortex sheets from up and down the train are rolled up to form two recirculation bubbles in the wake flow. Centers of the time-averaged bubbles in the recirculation region are parallel to the length of the train after a distance of $x/L \approx 0.35$ from the tip of the nose. This flow has strong unsteady vortex shedding, which influences the stability of the instantaneous recirculation bubbles. Snapshots of these bubbles show that their sizes are not constant and their centers are not fixed in space. Figure 8 shows two snapshots of the isosurface of the pressure with a time difference $\Delta t^* = 0.04$. The value of the pressure is -0.4 Pa. The wake structures are very different from time to time proving that the flow is highly unsteady. There is only a small portion of the upper recirculation bubble with a length of about $1D$ is steady as shown in Fig. 8. The lower part of the recirculation region is unsteady and the vortices are shed in an irregular fashion.

The two forms of flow instabilities are clearly shown here. Figure 9 shows the cross section of the test section at the middle of the length of the train at four different times with a time difference of $\Delta t^* = 0.04$. It is colored by the magnitude of the velocity. It shows the shedding of the large-scale vortices and also the small-scale vortex tubes due to the high frequency instability in the shear layers.

In case of 35^o side wind yaw angle, the flow structure is more complicated. Two

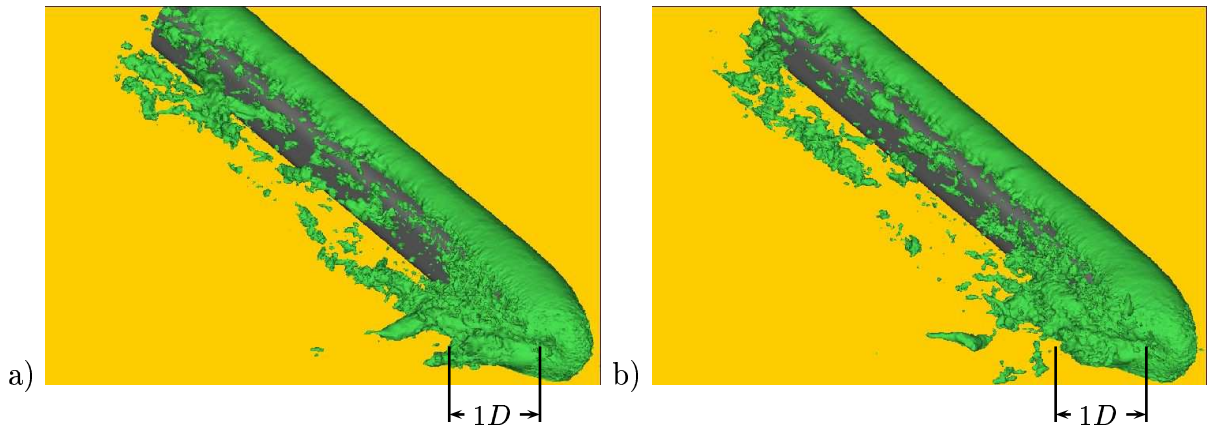

Figure 8: Isosurface of the instantaneous pressure showing the instantaneous wake structures in case of 90^o side wind yaw angle. The value of the static pressure is -0.4 Pa. The time difference between the two pictures is $\Delta t^* = 0.04$.

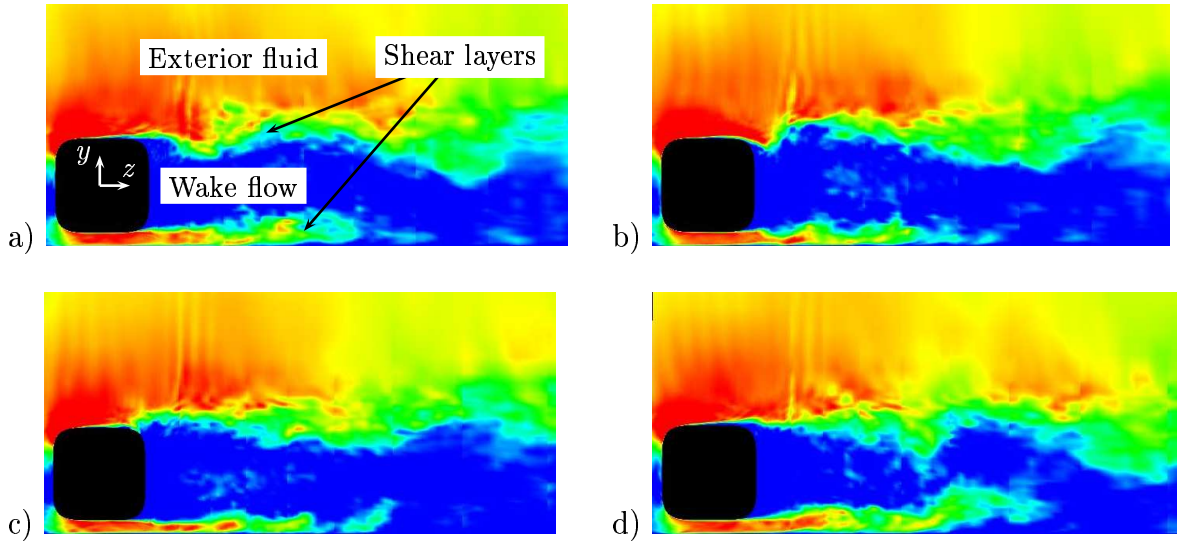

Figure 9: Cross-section at the middle of the train colored by the magnitude of the velocity showing the different flow instabilities in case of 90^o yaw angle.

flow regimes exist. The flow changes along the train length from the well-known steady slender body flow, where pairs of steady line vortices form the wake flow to unsteady vortex shedding. Figure 10 shows the instantaneous wake structures through the isosurface of the instantaneous pressure. The value of the pressure is -0.4 Pa. The time difference between the snapshots is 1 sec ($\Delta t^* = 8$).In contradictory to previous experimental observations, we found that vortices shed from the upper surface are not mirror images of the ones shed from under the train. The upper vortex shows strong steadiness along a length of about

$5D$ from its onset on the nose of the train. The strong vortex needs a length of about $1D$ to undergo transition from a steady to an unsteady regime. It becomes fully unsteady after a length of $6D$, where three-dimensional vortices are shed in the wake flow. The upper vortex remains attached to the surface of the train along the steady part. Then it detaches from the surface and another vortex starts to emerge.

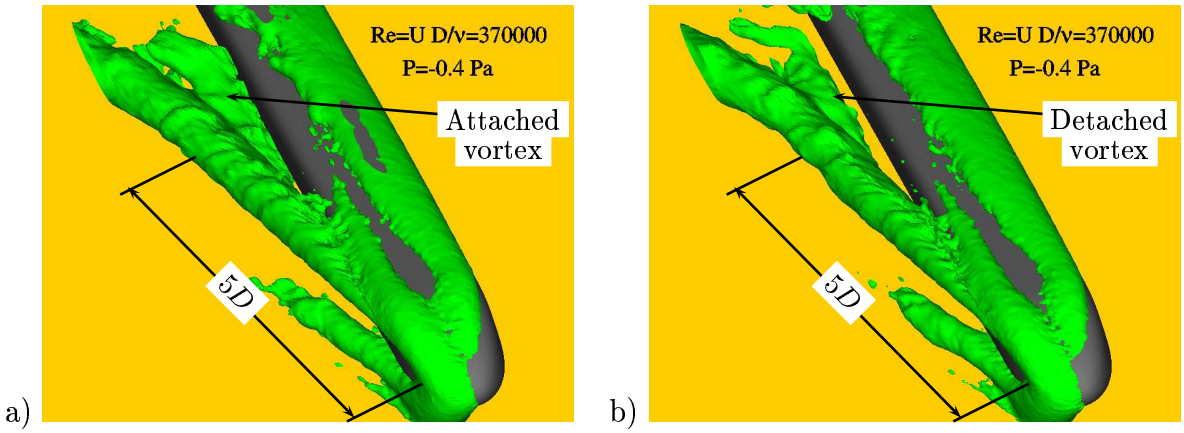

Figure 10: Isosurface of the instantaneous pressure showing the instantaneous wake structures in case of 35^o side wind yaw angle. The value of the static pressure is -0.4 Pa. The time difference between the two pictures is $\Delta t^* = 8$.

The lower vortices in the wake flow are weak and they are unsteady. Along the part of the train where the upper vortices are steady and attached to the surface of the train, many unsteady vortices are shed from the under body. The core of these vortices move in a horizontal plane parallel to the floor. They attaches and detaches to the surface of the train in a certain frequency. Figure 10a shows an attached vortex which is fully detached from the surface in Fig. 10b.

The instability and the movement of the wake vortices at both the 90^o and the 35^o yaw angles disturb the instantaneous train surface pressure. Typical aerodynamic force coefficients are shown in Figs. 11a and b. The time-averaged value of the side force coefficient does not change much with changing the yaw angle. This is due to the high stagnation pressure on the streamwise face next to the side wall and the lower pressure in the lee-side face resulting from the formation of the wake vortices in the case of the 35^o side-wind yaw angle. On the other hand, a lower lift coefficient is obtained for the 90^o side wind yaw angle. This is due to the lower pressure that forms on the upper face of the train in the case of the 90^o side wind yaw angle.

To determine the frequencies of the different flow motions, autopower spectra of the time varying signals of the force coefficients are computed. Figures 11c and d show these spectra for the side and the lift force coefficients, respectively. The dominating flow

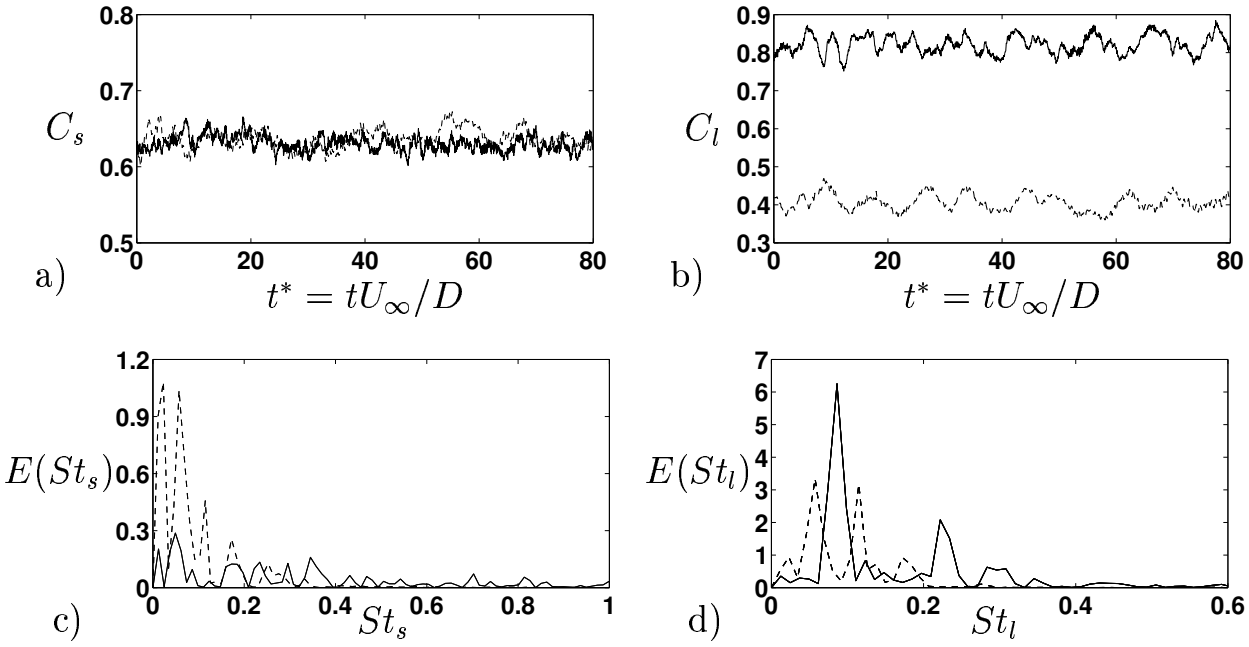

Figure 11: (a) and (b) are the side and lift force coefficients, respectively. (c) and (d) are the autopower spectra of the side and the lift force coefficients, respectively. 90^o yaw angle (solid line); 35^o yaw angle (dashed line)

frequencies for the 35^o side-wind yaw angle are confined in a narrow band of frequencies ($0.04 < St_s < 0.2$ and $0.05 < St_l < 0.2$) while the dominating frequencies for the 90^o side-wind yaw angle are spread out in a wide range of frequencies ($0.04 < St_s < 0.9$ and $0.1 < St_l < 0.5$). These frequency spectra reflect the difference in flow behavior for the large and small side wind yaw angles. In the case of the large yaw angles, the flow is dominated by unsteady vortex shedding with higher frequencies. In contrast, at low side-wind yaw angles, the flow is similar to flow around a slender body, where attachment and detachment of wake vortices dominate over the unsteady vortex shedding. The frequencies of these motions are lower than the unsteady shedding frequencies.

9 CONCLUSIONS

LES was successfully employed to predict the side wind flow around a generic train. The LES results are in a good agreement with existing experimental data. The side-wind flow at a 90^o yaw angle is dominated with unsteady vortex shedding while the side-wind flow at lower yaw angles changes from that associated with a slender body to unsteady shedding. At low yaw angles the underbody flow rolls up to produce line vortices at successive points along the length of the train. These vortices are highly unsteady. The upper-side vortices in the wake flow are much stronger and more stable than the lower ones.

10 ACKNOWLEDGMENTS

This work was supported by the Swedish Agency for Innovation System (VINNOVA), Bombardier Transportation and Scania. Computer time on HPC2N (High performance computing center north), NSC (National supercomputer center in Sweden), HIVE supercomputer at SWEGRID, and the HELIOS supercomputer provided by UNICC at Chalmers are gratefully acknowledged.

REFERENCES

[1] C.J. Baker. Some complex applications of the wind loading chain. *Journal of Wind Engineering and Industrial Aerodynamics*, 91:1791–1811, 2003.

[2] C.J. Baker, J. Jones, F. Lopez-Calleja, and J. Munday. Measurements of the cross wind forces on trains. *Journal of Wind Engineering and Industrial Aerodynamics*, 92:547–563, 2004.

[3] T. W. Chiu. Prediction of the aerodynamic loads on a railway train in a cross-wind at large yaw angles using an integrated two- and three-dimensional source/vortex panel method. *Journal of Wind Engineering and Industrial Aerodynamics*, 57:19–39, 1995.

[4] T. W. Chiu and L. C. Squire. An experimental study of the flow over a train in a crosswind at large yaw angles up to 90°. *Journal of Wind Engineering and Industrial Aerodynamics*, 45:47–74, 1992.

[5] J. M. Copley. The three-dimensional flow around railway trains. *Journal of Wind Engineering and Industrial Aerodynamics*, 26:21–52, 1987.

[6] M. Suzuki, K. Tanemoto, and T. Maeda. Aerodynamic characteristics of train/vehicles under cross winds. *Journal of Wind Engineering and Industrial Aerodynamics*, 91:209–218, 2003.

[7] U. Hoppmann, S. Koenig, T. Tielkes, and G. Matschke. A short-term strong wind prediction model for railway application: design and verification. *Journal of Wind Engineering and Industrial Aerodynamics*, 90:1127–1134, 2002.

[8] B. Diedrichs. On computational fluid dynamics modeling of crosswind effects for high-speed rolling stock. *IMechE*, 217(F):203–226, 2003.

[9] F. Durst W. Khier, M. Breuer. Flow structure around trains under side wind conditions: a numerical study. *Computers & Fluids*, 29:179–195, 2000.

[10] H. Hemida. Large-eddy simulation of the flow around simplified high-speed trains under side wind conditions. Thesis for Licentiate of Engineering 06/6, Division of

Fluid Dynamics, Dept. of Applied Mechanics, Chalmers University of Technology, Gothenburg, Sweden, 2006.

[11] S. Krajnović and L. Davidson. Large eddy simulation of the flow around an Ahmed body. In *2004 ASME Heat Transfer/Fluids Engineering Summer Conference*, Charlotte, North Carolina, USA, 2004.

[12] S. Singh and S. Mittal. Flow past a cylinder: shear layer instability and drag crisis. *Int. J. Num. Meth. Fluids*, 47:75–98, 2005.

[13] G. Kravchenko and P. Moin. Numerical studies of flow over a circular cylinder at Re=3900. *Physics of Fluids*, 12(2):403–417, 2000.

[14] R. Mittal and P. Moin. Stability of upwind-biased finite difference schemes for large-eddy simulation of turbulent flows. *AIAA Journal*, 35(8):1415–1417, 1997.

[15] G.S. Constantinuescu and K.D. Squires. LES and DES investigations of turbulent flow over a sphere at Re=10,000. *Journal of Flow, Turbulence and Combustion*, 70:267–298, 2003.

[16] S. Krajnović and L. Davidson. Flow around a simplified car, part 1: Large-eddy simulation. *ASME: Journal of Fluids Engineering*, 127:907–918, 2005.

[17] S. Krajnović and L. Davidson. Flow around a simplified car, part 2: Understanding the flow. *ASME: Journal of Fluids Engineering*, 127:919–928, 2005.

[18] H. Nilsson and L. Davidson. CALC-PVM: A parallel multiblock SIMPLE multiblock solver for turbulent flow in complex domains. Technical report, Dept. of Thermo and Fluid Dynamics, Chalmers University of Technology, Gothenburg, 1998.

[19] H. Hemida, S. Krajnović, and L. Davidson. Large-eddy simulations of the flow around a simplified high speed train under the influence of a cross-wind. In *17th AIAA Computational Fluid Dynamics Conference*, Toronto, Ontario, CANADA 6-9 Jun, 2005.